nature physics

Article

https://doi.org/10.1038/s41567-023-02380-1

Bragg glass signatures in Pd_xErTe_3 with X-ray diffraction temperature clustering

Received: 22 September 2022

Accepted: 18 December 2023

Published online: 9 February 2024

Check for updates

Krishnanand Mallayya[1], Joshua Straquadine[2,3], Matthew J. Krogstad[4,5], Maja D. Bachmann[2,3], Anisha G. Singh[2,3], Raymond Osborn[4], Stephan Rosenkranz[4], Ian R. Fisher[2,3] & Eun-Ah Kim[1,6]

The Bragg glass phase is a nearly perfect crystal with glassy features predicted to occur in vortex lattices and charge-density-wave systems in the presence of disorder. Detecting it has been challenging, despite its sharp theoretical definition in terms of diverging correlation lengths. Here we present bulk probe evidence supporting a Bragg glass phase in the systematically disordered charge-density-wave material of Pd_xErTe_3. We do this by using comprehensive X-ray data and a machine-learning-based analysis tool called X-ray diffraction temperature clustering (X-TEC). We establish a diverging correlation length in samples with moderate intercalation over a wide temperature range. To enable this analysis, we introduced a high-throughput measure of inverse correlation length that we call peak spread. The detection of Bragg glass order and the resulting phase diagram advance our understanding of the complex interplay between disorder and fluctuations. Moreover, the use of our analysis technique to target fluctuations through a high-throughput measure of peak spread can revolutionize the study of fluctuations in scattering experiments.

The interplay between disorder and fluctuations can result in complex new phases, such as spin glasses, recently celebrated through a Nobel prize[1]. Although theoretical frameworks for understanding such complex phases can have far-reaching implications, it can be challenging to untangle the subtleties of this interplay from experimental data when finite experimental resolution and noise can obscure comparisons with idealized theoretical predictions. The Bragg glass is an example of such an elusive novel phase[2,3]. It is an algebraically ordered glass, which can appear as ordered as a perfect crystal, but whose Bragg peak intensities diverge as power laws[2,4–13]. However, with the experimental resolution cutting off the divergence in actual data, it can be challenging to detect a Bragg glass. Although the Bragg glass has been proposed for charge-density-wave (CDW) systems[9,10] and vortex lattices[14], unambiguous direct evidence has, so far, been limited to vortex lattices[15–19]. Since the lattice periodicity in a vortex lattice is controlled by the magnetic field, the magnetic-field-independent width of the rocking curve has been used as evidence for the absence of an intrinsic length scale and the underlying algebraic order[15]. A scanning tunnelling microscopy (STM) probe on 1T-TaS_2 also revealed the Bragg glass decay of translational order in a vortex lattice of CDW topological defects[20]. However, the evidence of Bragg glass phenomena in incommensurate CDW systems with emergent, system-specific periodicity is suggestive at best and limited to STM studies of $NbSe_2$ (ref. 21) and Pd_xErTe_3 (ref. 22). Hence, whether an algebraically ordered CDW phase can exist as a bulk phase in a CDW system or whether CDWs always respond to disorder as, for example, a vestigial nematic with a short correlation length[23] remains an open problem.

In this work, we present the first bulk signature supporting a Bragg glass phase in a systematically disordered CDW material, namely, Pd_xErTe_3, using comprehensive single-crystal X-ray scattering and a novel machine-learning-based method of data analysis called X-ray diffraction temperature clustering (X-TEC) (introduced elsewhere[24]).

[1]Department of Physics, Cornell University, Ithaca, NY, USA. [2]Geballe Laboratory for Advanced Materials and Department of Applied Physics, Stanford University, Stanford, CA, USA. [3]Stanford Institute for Materials and Energy Sciences, SLAC National Accelerator Laboratory, Menlo Park, CA, USA. [4]Materials Science Division, Argonne National Laboratory, Lemont, IL, USA. [5]Advanced Photon Source, Argonne National Laboratory, Lemont, IL, USA. [6]Department of Physics, Ewha Womans University, Seoul, South Korea. e-mail: eun-ah.kim@cornell.edu

Specifically, we provide evidence indicating the vanishing intrinsic length scale by tracking the temperature and momentum dependence of all the CDW peaks in a reciprocal-space volume spanning 20,000 Brillouin zones (BZs) with the help of X-TEC. To the best of our knowledge, this is the first time CDW fluctuations have been analysed from more than a handful of peaks. The statistics afforded by such an unprecedented comprehensive analysis of the CDW peak width enables an accurate assessment of CDW correlation lengths by eliminating contributions to the observed peak width from crystal imperfections, and statistically minimizing errors near the resolution limit. The resulting phase diagram establishes the Bragg glass to be the dominant phase, aligning with the onset of the transport anisotropy previously observed[25].

The notion that a quasi-long-range ordering of vortex lattices and CDWs is possible in the form of Bragg glass in the presence of disorder[2–4] was a surprising theoretical prediction contradicting the long-standing wisdom that order parameters that linearly couple with a disorder potential are destined to be short ranged at best[26]. The key difference lies in whether the phase fluctuation is allowed to indefinitely grow or the phase is compactly defined within [0, 2π). When considering a phase linearly coupling to the disorder potential, it has been shown that phase fluctuations can arbitrarily grow to overcome the elastic restoring energy, resulting in short-range correlations below four dimensions[26]. However, it was noted[4] that the phase of periodic states such as CDWs and vortex lattices should be compactly defined within [0, 2π); this compactness keeps the impact of the disorder potential in check. Specifically, the disorder-averaged potential energy depends on the exponential of phase fluctuations, allowing for quasi-long-range order in phase correlations in three dimensions[2–4] (Supplementary Section A). Evidence for the divergence of correlation length with such quasi-long-range order would be the vanishing width of the structure factor peaks associated with the periodicity[9,10]. Since the vortex or CDW phase is well defined within [0, 2π) only in the absence of dislocations[5–7], the observation of such an absence[21,22] establishes a necessary—but not a sufficient—condition for a Bragg glass.

There are many challenges in making direct observations of Bragg glass phenomena in CDW systems. First, for a systematic understanding of the role of disorder, a material family with adjustable disorder is needed. Second, for a reliable separation of real-life issues such as crystal imperfections and finite resolution contributing to the peak width from the sought-after fluctuation effects, a large volume of comprehensive data is imperative. Finally, for a reliable analysis of such large volumes of comprehensive data, a new approach towards data analysis is critical. We turn to Pd_xErTe_3 to address the first issue—the material system challenge[22,25,27]. Pristine $ErTe_3$ is a member of the rare-earth tritelluride family with nearly square Te nets and a glide plane distinguishing the two in-plane directions a and c (Fig. 1a). It hosts a unidirectional CDW ordering (CDW-1, along the c axis) below a critical temperature T_{c1} and an orthogonal unidirectional CDW ordering (CDW-2, along the a axis) below T_{c2}, where $T_{c2} < T_{c1}$ due to weak orthorhombicity[28]. Pd intercalation provides localized disorder potentials at random sites, making Pd_xErTe_3 a model system to study emergent phases from the suppression of long-range CDW order[22,25]. Transport measurements in the pristine sample have revealed the onset of anisotropy in resistivity between the a and c axes at the CDW transition temperature[25,29]. Increasing intercalation lowers the onset temperature for transport anisotropy[25]. Although this reveals the broken C_4 symmetry, two possible candidates for the disordered CDW phase remain open: a short-range-ordered CDW forming a vestigial nematic phase pinned by a weak symmetry-breaking field and a Bragg glass phase characterized by quasi-long-range CDW order with divergent power-law correlations.

We overcome the second challenge of the data volume by taking X-ray temperature series data for single crystals of Pd_xErTe_3 at different intercalation strengths ($x = 0$, 0.5%, 2.0%, 2.6% and 2.9%). We utilize highly efficient methods for collecting the total X-ray scattering over large volumes of reciprocal space recently developed at Sector 6-ID-D at the Advanced Photon Source[30]. In each measurement, a crystal is continuously rotated through 360° at a rate of 1° s^{-1} as images are collected on a FAST area detector (PILATUS 2M CdTe) every 0.1 s, with a monochromatic incident X-ray energy of 87 keV. Three rotations are required to fill in gaps between the detector chips. Uncompressed, the volume of raw data is over 100 GB. Although the data volume is reduced by an order of magnitude after transforming the images into reciprocal-space meshes, these meshes include over 10,000 BZs and approximately 5×10^8 bins containing data. Such volumes are collected at a series of temperatures from 30 to 300 K, controlled by a helium/nitrogen cryostream. During the transformation of images to reciprocal space, one should ensure that the orientation is properly maintained at each temperature (Supplementary Section K).

Finally, we overcome the challenge of data analysis through a scalable extraction of theoretically relevant features using a machine learning algorithm called X-TEC[24]. In the X-ray scattering data, the CDW lattice distortions manifest as satellite peaks around each Bragg peak (Fig. 1b). We focus on the temperature evolution of two features associated with the CDW peaks (Fig. 1c): peak height and peak width. In the long-range-ordered CDW of the pristine sample, the temperature dependence of peak heights is sufficient to reveal the order parameter and transition temperature (T_c). However, disorder can often broaden the transition. Moreover, in a Bragg glass, the temperature dependence of the peak height does not reveal a clear onset behaviour. This is because even after the breakdown of the Bragg glass order, a non-vanishing superlattice peak intensity continues to persist to higher temperatures due to thermal and disorder fluctuations to the CDW order (Fig. 1d, first row of the table). On the other hand, the peak width of the CDW peaks (Fig. 1c, Γ) should vanish on transition into both long-range-ordered and Bragg glass phases (Fig. 1d, second row of the table), whereas a short-range-ordered phase, such as a vestigial nematic, will show a finite width down to the lowest temperatures (Supplementary Section C). Invariably, finite experimental resolution and finite amount of crystalline defects present in the samples will mask this difference. However, with enough statistics over a range of temperatures, the temperature dependence of the width can be extrapolated to the vanishing point and allow for the determination of the Bragg glass transition temperature T_{BG} (Fig. 1d, second row). Hence, the Bragg glass phase is a phase that appears like long-range-ordered phase despite the presence of a weak disorder. The effect of disorder can be evident from the asymmetry between a pair of CDW satellite peaks. As shown in Supplementary Section D, disorder pinning is required for such asymmetry[31]. Therefore, we anticipate asymmetric pairs of CDW peaks with a vanishing width in a Bragg glass phase.

Manually tracking the three features of the disordered CDW from large datasets (Fig. 1e) presents a daunting challenge; hence, there is the need for an automated machine learning approach like X-TEC. At the core of the X-TEC algorithm is Gaussian mixture model clustering to identify distinct temperature trajectories from the X-ray data. This is achieved by representing the intensity–temperature trajectory at each $\vec{q}$ in reciprocal space as $\{I_{\vec{q}}(T_i)\}$ spanning d number of temperatures $\{T_1 \ldots T_d\}$ (Fig. 1e, $d = 19$) as a point in d-dimensional space (Supplementary Fig. 2 shows a two-dimensional projection of this space). From this distribution in hyperspace, the Gaussian mixture model identifies a number of distinct clusters and assigns points to each one. From these cluster assignments, we can identify distinct intensity–temperature trajectories present in the data (Fig. 1g), thereby revealing the physically interesting ones, such as those representing the temperature dependence of the order parameters.

We first benchmark the X-TEC outcomes against known results for the pristine $ErTe_3$ data (Fig. 2a). The collection of raw data fed into X-TEC yields two well-defined CDW transitions in a matter of minutes (Supplementary Section F provides details on X-TEC processing). From the mean trajectories of the intensities in these two clusters, we can

https://doi.org/10.1038/s41567-023-02380-1

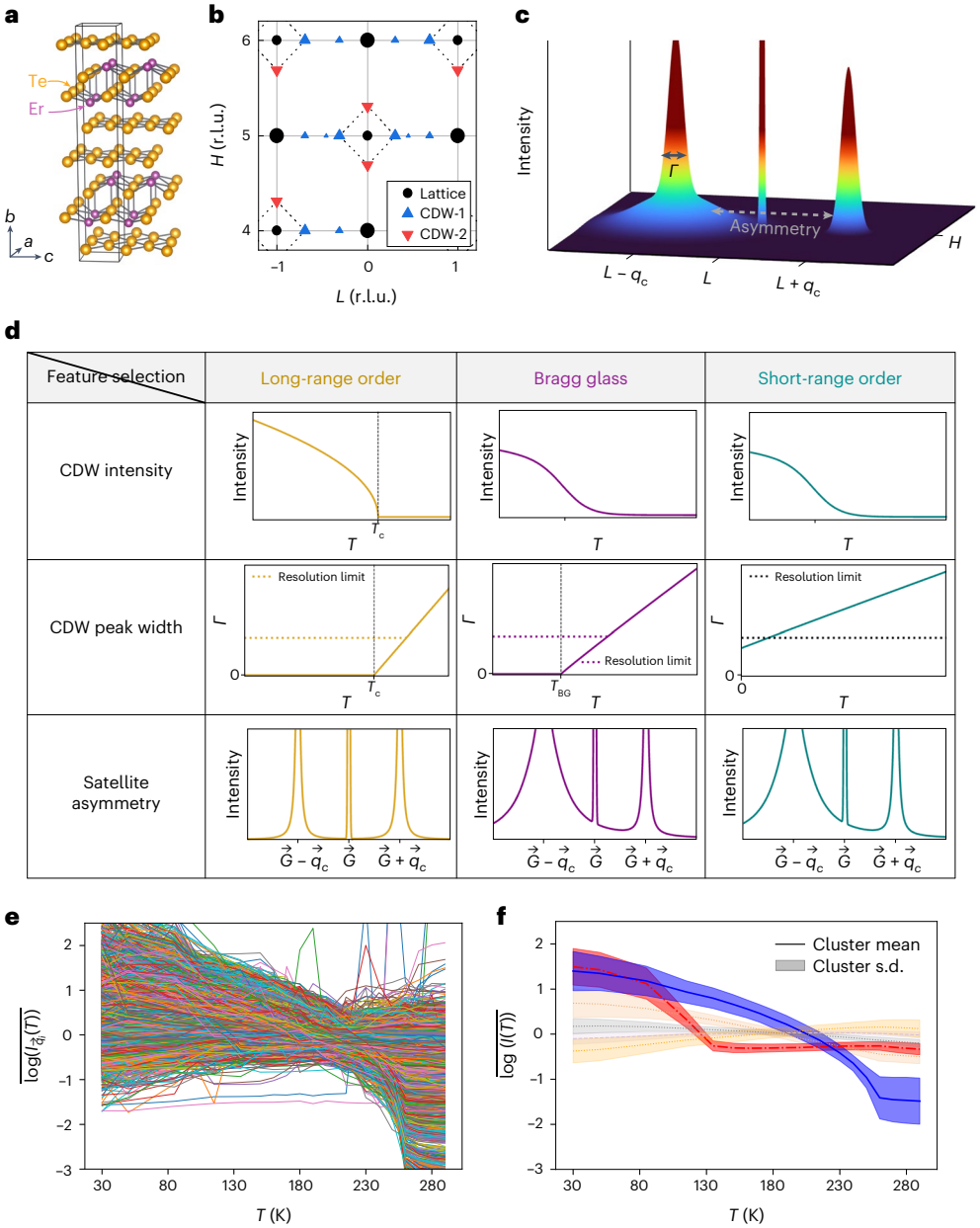


Fig. 1 | CDWs in Pd_xErTe_3. a, Crystal structure of pure $ErTe_3$. The Te planes have approximately square geometry. The crystal belongs to the *Cmcm* space group, *b* denotes the out-of-plane axis, and *a* and *c* are the in-plane axes. **b**, Schematic[25] showing the Bragg peaks (circles) and CDW peaks (triangles) in the in-plane (a^*–c^*) reciprocal space. The satellite peaks of CDW-1 (up triangle) and CDW-2 (down triangle) are aligned along the c^* and a^* axes, respectively. **c**, Schematic for the in-plane (a^*–c^*) intensity distribution of the pair of CDW satellite peaks (at $(H, L \pm q_c)$) around a Bragg peak (at (H, L)), with the following three features of interest: the intensity of the peak, the width of the peak Γ (solid arrow) and the asymmetry in the diffuse scattering surrounding the satellite peaks (dashed arrow). **d**, Table summarizing the diagnostics for classifying the three phases. The first row describes the CDW intensity–temperature trajectory. Only the pristine sample with a long-range order exhibits a sharp onset, marking the transition temperature T_c. On the other hand, one cannot distinguish Bragg glass from short-range order as even after the breakdown of Bragg glass order with increasing temperature, short-ranged fluctuations persist (due to disorder pinning) and contribute to the CDW intensity. The second row illustrates a simplified temperature dependence of the CDW peak width Γ. The width is zero in the long-range-ordered phase below T_c of the pristine sample, as well as in the Bragg glass phase below the transition temperature T_{BG_1} of the disordered sample (Supplementary Section B). The vanishing width distinguishes Bragg glass from short-range order. The observed width levels off at the resolution limit (dotted line). The third row illustrates the asymmetry in the diffuse scattering intensity across a Bragg peak. The asymmetry distinguishes pristine (long-range order) from the intercalated (Bragg glass and short-range order) sample as its presence indicates disorder pinning (Supplementary Section C). **e**,**f**, Illustration of X-TEC to cluster distinct intensity–temperature trajectories $I(T)$ given the intensity–temperature trajectory $I_{\vec{q}}(T)$ of the pristine $ErTe_3$ sample at various momenta $\vec{q}$ in reciprocal space. The raw trajectories at each $\vec{q}$ are rescaled as $\overline{\log[I_{\vec{q}}(T)]} = \log[I_{\vec{q}}(T)] - \langle \log[I_{\vec{q}}(T)] \rangle_T$ (**e**). X-TEC clusters the trajectories (with colour assignments to identify each cluster). The distinct trajectories $I(T)$ and their standard deviation (s.d.) are shown in **f**.

identify two transition temperatures, namely, $T_{c1} \approx 260$ K and $T_{c2} \approx 135$ K. The transition temperatures identified by X-TEC are consistent with those determined from transport anisotropies[25]. Turning to where the clusters are located in reciprocal space, we find that the two intensity clusters correspond to the CDW-1 and CDW-2 peaks, whose K dependence is consistent with known selection rules (Fig. 2b,c). Both CDW-1 and CDW-2 peaks are sharp, as expected for three-dimensional CDW order, and therefore satisfy the dimensionality condition necessary

https://doi.org/10.1038/s41567-023-02380-1

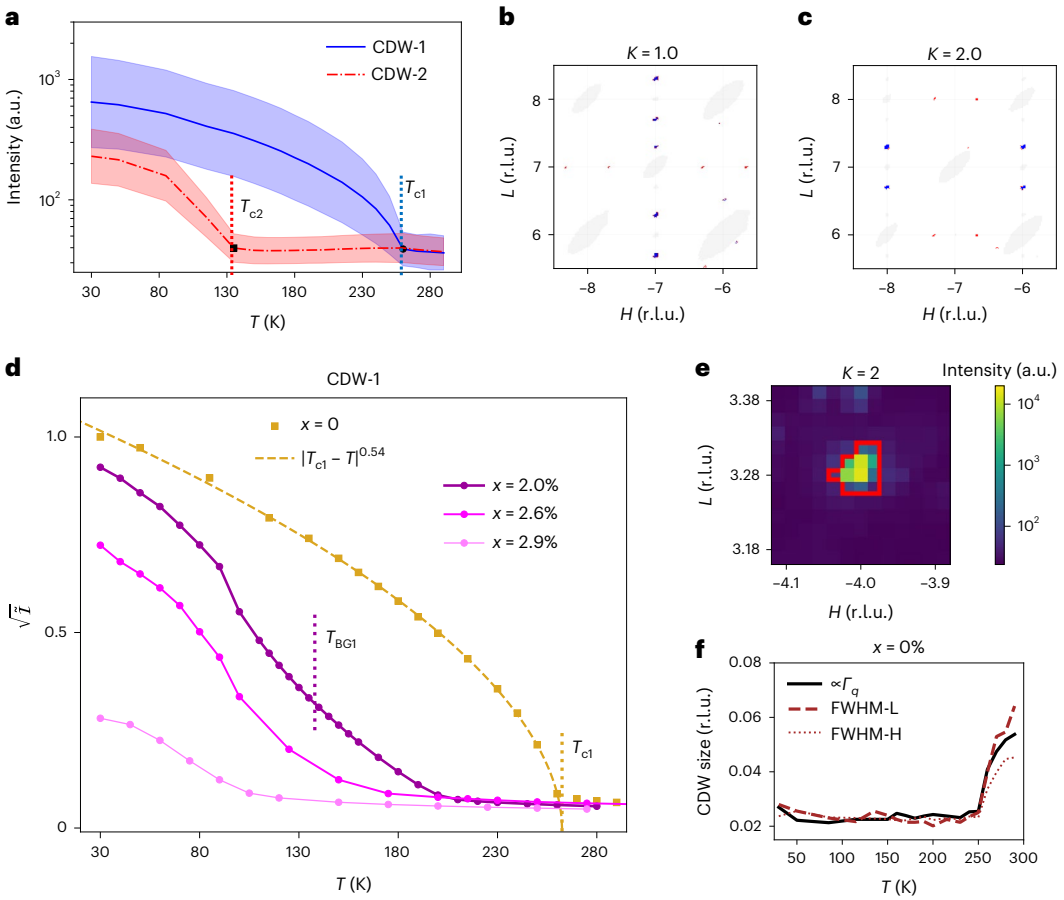


Fig. 2 | Benchmarking the X-TEC analysis of CDW peak height and peak spread of pristine $ErTe_3$. a, X-TEC reveals the intensity clusters corresponding to the two trajectories of the CDW order parameter, colour coded as red and blue. The lines describe the mean and the shaded regions describe one standard deviation of the intensities within each cluster. The estimated transition temperatures $T_{c1} \approx 262$ K for CDW-1 and $T_{c2} \approx 135$ K for CDW-2 are consistent with the temperatures from transport measurements provided elsewhere[25]. a.u., arb. units. **b**,**c**, A small region of reciprocal space where momenta whose intensity trajectory belongs to the red and blue cluster assignments in **a** are labelled as red and blue pixels, respectively. The red (blue) pixels conform to the CDW-1 (CDW-2) peaks along the c^* (a^*) axis. The light-grey pixels correspond to Bragg peaks and their diffuse scattering. The three-dimensional structure of the peaks is apparent from the $K = 1$ (odd) plane (**b**) and $K = 2$ (even) plane (**c**) that show two different patterns reflecting the *Cmcm* selection rules governing the Bragg peaks. **d**, CDW-1-peak-averaged intensity (peak height) for Pd_xErTe_3 at intercalation strengths of $x = 0$, 2.0%, 2.6% and 2.9%. The value of $\tilde{I}$ is obtained from the average of all the intensities in the CDW-1 cluster (~3,000 peaks), from which we subtract the background intensity contribution. The $\tilde{I}$ values for all the samples are normalized with the maximum value for $x = 0$ for comparison. $\sqrt{\tilde{I}(T)}$ for $x = 0$ fits well by a power law, namely, $\propto (T_{c1} - T)^{\beta}$, giving $T_{c1} \approx 262$ K and $\beta = 0.54$, matching the Bardeen–Cooper–Schrieffer order parameter exponent. The Bragg glass transition temperature T_{BG_1} for $x = 2.0\%$ and $x = 2.6\%$ is estimated from the peak-width analysis shown in Fig. 3e,f. All the solid lines are guides to the eyes. **e**, CDW-1 peak intensity distribution in the H–L plane ($K = 2$) for the $x = 0$ sample at $T = 30$ K. The red boundary for the CDW-1 peak is estimated by X-TEC (pixels inside the boundary belong to the CDW-1 cluster). Within this boundary, the total intensity $I_{\vec{q}}^{\mathrm{Tot}}(T)$ and maximum intensity $I_{\vec{q}}^{\mathrm{Max}}(T)$ of the peak give the high-throughput measure of the peak spread $\Gamma_{\vec{q}}(T)$ (equation (1)). **f**, Peak spread (Γ) of the CDW peak in **e**, along with the full-width at half-maximum (FWHM) from linecuts along H (FWHM-H) and L (FWHM-L), at various T values for $x = 0$.

for a stable Bragg glass phase[32,33]. In the rest of the paper, we focus on the CDW-1 peaks with a higher transition temperature matching the expectations of the Bardeen–Cooper–Schrieffer order parameter in the pristine sample (Fig. 2d).

Repeating the X-TEC analysis on all the intercalated samples, one can readily extract our first feature of interest: the temperature trajectory of the CDW peak intensity (peak height) (Fig. 2d). We show the average trajectory of all the CDW-1 peaks at various intercalation levels. Increasing intercalation suppresses the overall intensity of modulations, but, more importantly, it spreads out the intensity distribution as a function of temperature, leaving a long tail up to higher temperatures. The long tail due to pinned CDW fluctuations at the intercalants[34] hinders a clean determination of the putative Bragg glass transition[2–4] from the temperature dependence of the peak intensities. On the other hand, an STM study on Pd_xErTe_3 (ref. 22) has shown the absence of free dislocations, which is necessary for a Bragg glass, for moderate levels of intercalation ($x \lesssim 2\%$) at a base temperature of $\lesssim$1.7 K.

To target the unambiguous signature of a Bragg glass, we now turn to our second feature of interest, namely, the peak width. The objective is to separate three sources of CDW peak broadening with confidence: (1) instrumental resolution, (2) finite CDW correlation lengths and (3) crystal imperfections. Our approach is to use the $\vec{q} \equiv (H, K, L)$ dependence of the peak broadening since only crystal imperfections would result in a (quadratic) momentum dependence across the BZs (Supplementary Section E). This strategy requires measuring the peak widths over a sufficiently large number of BZs. Although our experimental setup can give us ready access to XRD data across 20,000 BZs, the traditional approach for extracting peak widths cannot use such comprehensive information. Specifically, the traditional approach for extracting the peak width of fitting a linecut of high-resolution data is not scalable (Supplementary Section G). This forces researchers to an ad hoc choice of a handful of peaks, ruling out statistically meaningful $\vec{q} \equiv (H, K, L)$ analysis. Moreover, aiming to identify the power-law tails of Bragg glass from fitting the peaks is not feasible as the peaks are

https://doi.org/10.1038/s41567-023-02380-1

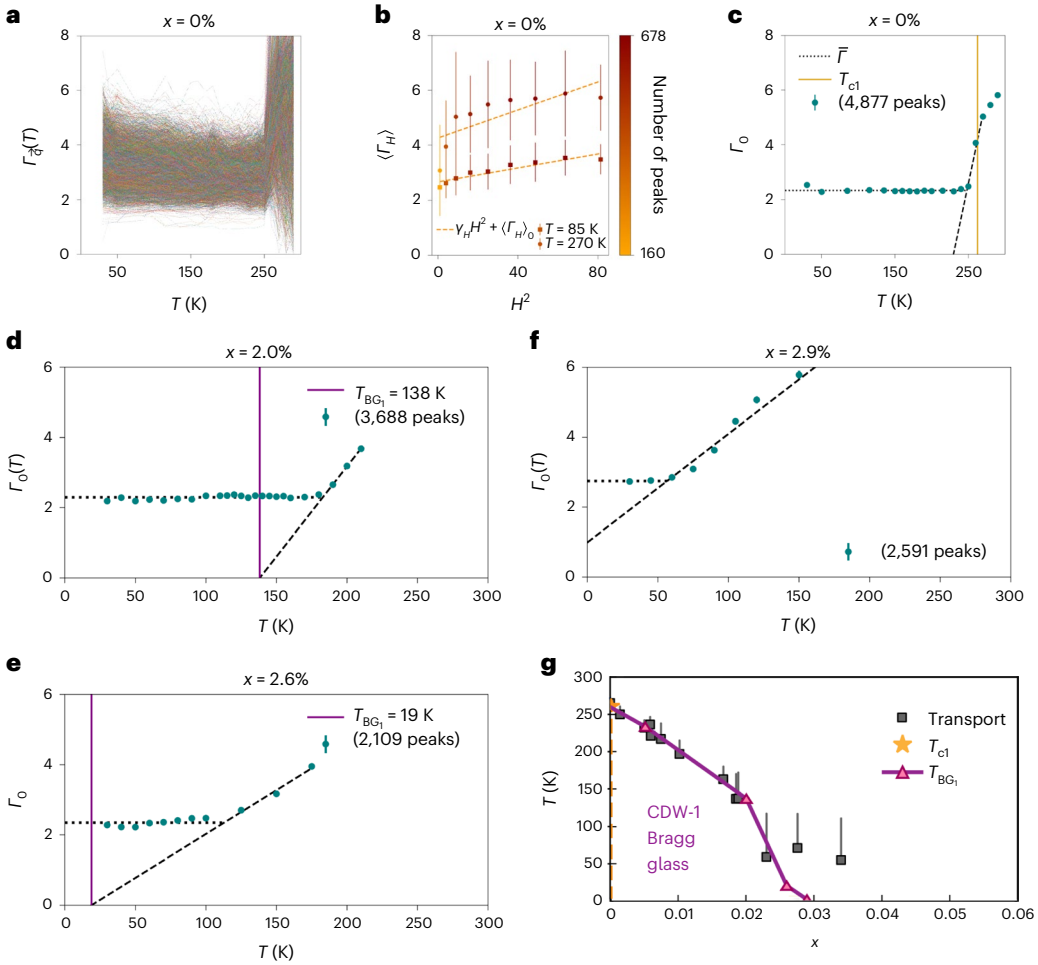


Fig. 3 | Momentum-independent peak spread and Bragg glass transition. **a**, Peak spread $\Gamma_{\vec{q}}(T)$ of all the CDW-1 peaks in the $x = 0$ data. **b**, Quadratic momentum (H^2) dependence of $\Gamma_{\vec{q}}(T)$. $\langle\Gamma_H\rangle$ (symbols) is obtained by averaging $\Gamma_{\vec{q}}$ over values of K and L that share the same $|H|$. The symbols show the mean ± one standard deviation. The markers are colour coded, and the colour bar indicates the number of peaks determining the statistics of each marker. **c**, From the erratic and broad distribution of $\Gamma_{\vec{q}}(T)$ in **a**, the momentum-independent spread Γ_0 extracted from the three-dimensional quadratic fit (equation (2)) shows a T-independent (resolution-limited) spread below T_{c1}, where $T_{c1} = 262$ K (Fig. 2d). The symbols give the fit estimate, and the error bars give the 95% confidence bounds on Γ_0 estimated from 4,877 peaks. The dashed line shows the linear extrapolation (equation (3)) to vanishing width. **d**–**f**, The $\vec{q}$-independent broadening of the CDW-1 peak spread, $\Gamma_0(T)$, extracted by fitting their $\Gamma_{\vec{q}}$ values to a quadratic function of $\vec{q}$ (equation (2)) for $x = 2.0\%$ (**d**), 2.6% (**e**) and 2.9% (**f**). The symbols give the fit estimate, and the error bars give the 95% confidence bounds on Γ_0 estimated from 3,688 (2.0%), 2,109 (2.6%) and 2,591 (2.9%) peaks. The dashed lines are a phenomenological fitting function (equation (3)) to extract CDW-1 Bragg glass temperature T_{BG_1}. The dotted lines mark the resolution limit $\overline{\Gamma}$ from the fit. We find a Bragg glass regime for the $x = 2.0\%$ and 2.6% samples by extracting T_{BG_1} (vertical solid lines) from extrapolating the broadening regime to zero spread. **g**, Our estimates for the transition temperatures T_{c1} for $x = 0$ (star symbol) and T_{BG_1} for $x > 0$ (up triangles) are overlaid on the phase diagram from the in-plane resistance anisotropy measurements (square symbols) from another work[25]. The lines are guides to the eyes. The CDW-1 long-range-ordered phase of $x = 0$ is indicated by the dashed orange line, and the CDW-1 Bragg glass phase lies below T_{BG_1} for $x > 0$.

sharp and span only 2–3 pixels (Supplementary Fig. 5). Instead, we have adopted a high-throughput approach, by combining the automatic X-TEC extraction of all the CDW peaks and using a new measure of peak width, namely, the peak spread

$$\Gamma_{\vec{q}}(T) \equiv \frac{I_{\vec{q}}^{\mathrm{Tot}}(T)}{I_{\vec{q}}^{\mathrm{Max}}(T)}, \qquad (1)$$

in units of number of pixels. Here $I_{\vec{q}}^{\mathrm{Tot}}(T)$ is the integrated intensity and $I_{\vec{q}}^{\mathrm{Max}}(T)$ is the maximum intensity (peak height) of the CDW peaks identified by X-TEC. The peak spread quantifies how many pixels the peak is effectively spread over (Fig. 2e). Although being consistent with the conventional estimates of peak width (Fig. 2f and Supplementary Section H), the spread as defined here possesses several merits compared with the traditional extraction of inverse correlation length. First, it is model independent. Second, it does not require high-resolution data. Third, it naturally integrates with X-TEC, which offers the peak boundaries for all the CDW peaks (Fig. 2e). Finally, when combined with X-TEC, $\Gamma_{\vec{q}}(T)$ can reveal the momentum and temperature evolution of peak widths over a large number of CDW peaks.

Armed with the new high-throughput measure of peak spread $\Gamma_{\vec{q}}(T)$, we single out the CDW fluctuation contributions by extracting the momentum-independent part of the peak spread by analysing $\Gamma_{\vec{q}}(T)$ across 20,000 BZs and the entire temperature range (Fig. 3a–c). Specifically, we fit the momentum dependence of $\Gamma_{\vec{q}}(T)$ at each temperature T to a quadratic function expected in the small $|\vec{q}|$ limit (Fig. 3b)[35–39]:

$$\Gamma_{\vec{q}\equiv(H,K,L)}(T) = \Gamma_0(T) + \gamma_H(T)H^2 + \gamma_K(T)K^2 + \gamma_L(T)L^2, \qquad (2)$$

https://doi.org/10.1038/s41567-023-02380-1

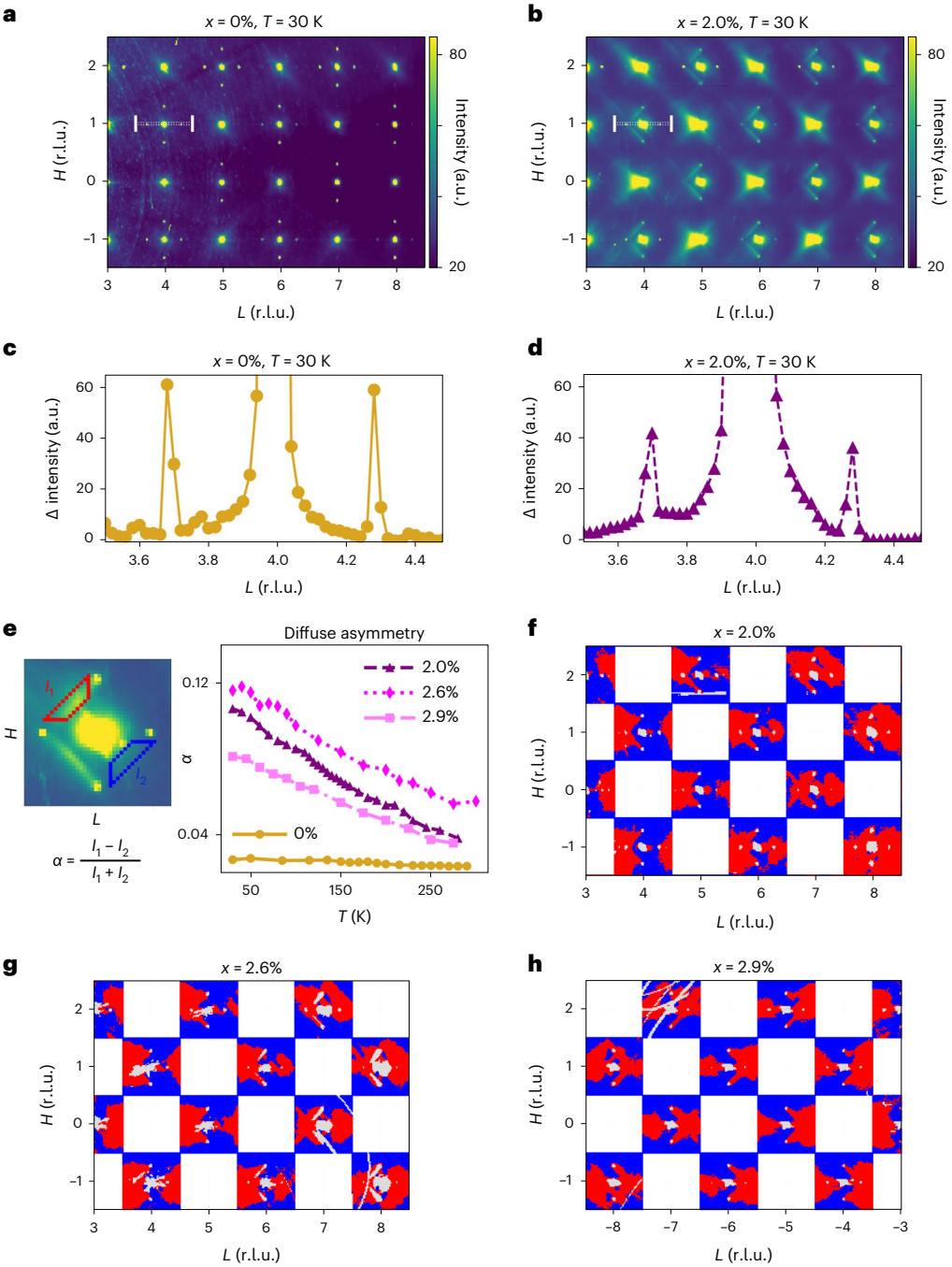


Fig. 4 | Intensity asymmetry of the CDW satellite peaks. a,**b**, X-ray intensity at $T = 30$ K, in the H–L plane with K (out-of-plane axis) averaged over all the values ($-20 \le K \le 20$), for the pristine sample ($x = 0$; **a**) and intercalated sample ($x = 2\%$; **b**). Only the intercalated sample shows a diffuse scattering that is asymmetrically distributed between the two satellite peaks, in the form of half-diamonds. The white horizontal dotted lines across a pair of CDW-1 satellite peaks mark the region along which a linecut is taken, as shown in **c** and **d**. **c**,**d**, Linecut intensities $I(L)$ for the pristine (**c**) and 2%-intercalated (**d**) sample at 30 K. Linecuts are along $3.5 \le L \le 4.5$ reciprocal lattice units (r.l.u.) with intensity averaged over $H \in [0.98, 1.02]$ (r.l.u.) and $K \in [-20, 20]$ (r.l.u.). **e**, Asymmetry in diffuse scattering, quantified by the ratio $\alpha = (I_1 - I_2)/(I_1 + I_2)$ for each satellite pair, where I_1 and I_2 are the intensities averaged within the upper-left arm (red boundary) and the lower-right arm (blue boundary), respectively. The plot shows the average value of α evaluated for the satellite diffuse diamonds of all the $H + L$ = odd Bragg peaks in reciprocal space in **a** and **b**. **f**–**h**, Two-cluster X-TEC results colour coded as red and blue, from the temperature trajectories of the diffuse scattering intensities of the intercalated sample with $x = 2.0\%$ (**f**), 2.6% (**g**) and 2.9% (**h**). The asymmetric distribution of red and blue clusters surrounding the CDW satellite peaks is systematically present in the three intercalated samples, clearly revealing the signature of disorder pinning. The intensities of CDW peaks and $H + L$ = odd Bragg peaks (white pixels, identified from a prior X-TEC analysis) are excluded from this two-cluster X-TEC, along with the $H + L$ = even Bragg peaks removed by a square mask (square white regions). a.u., arb. units.

where $\gamma_H(T)$, $\gamma_K(T)$ and $\gamma_L(T)$ quantify the momentum dependence at each temperature T along the a^*, b^* and c^* axes, respectively. In this way, the extracted momentum-independent width $\Gamma_0(T)$ would reflect the peak width solely due to CDW fluctuations (Supplementary Section H). Indeed, $\Gamma_0(T)$ extracted from ~3,000 peaks of the pristine sample drops and plateaus at the critical temperature T_{c1} (Fig. 3c), as expected for the long-range-ordered signal cut-off by finite experimental resolution (Fig. 1d).

This analysis reveals the emergence of a threshold temperature in intercalated samples (Fig. 3d–f), below which $\Gamma_0(T)$ becomes constant, signifying that the widths of the CDW peaks at these low temperatures are resolution limited. This resolution limit corresponds to an in-plane correlation length of ~20 nm. With the average distance between Pd atoms (~2 nm for $x = 2.9\%$ (ref. 25)) being smaller than the correlation length, this corresponds to a weak-pinning scenario. A finite-resolution limit is inevitable in any experiment, leaving behind the question of whether the system has long-range order beyond the resolution limit. To go beyond the resolution limit and find the point of vanishing peak width, we extrapolate $\Gamma_0(T)$ using an empirical formula:

$$\Gamma_0(T) = \overline{\Gamma} + \alpha(T - \beta)\Theta[T - \beta]. \quad (3)$$

Here $\Theta[t > 0] = 1$ is the Heaviside step function, and $\overline{\Gamma}$ (resolution limit), α and β are fitting parameters. The linear-in-T dependence of $\Gamma_0(T)$ is motivated as a first-order approximation of $\Gamma_0(T)$ near its vanishing limit. Although a series expansion of the width near T_{c1} is not strictly valid for the long-range order whose width vanishes as a power law in T near T_{c1}, the linear approximation will still extrapolate to give the vanishing width with a reasonable value (a lower bound) for T_{c1} when applied to temperatures close to T_{c1} (Fig. 3c). For the intercalated samples, the vanishing trend of the peak spread (Fig. 3d,e) is contrary to the predicted behaviour for disorder-pinned short-range CDW order where the peak spread increases with lowering temperature[40]. On the other hand, it supports a Bragg glass phase, as it is inevitable for the peak spread to vanish below the Bragg glass transition[10]. We estimate the Bragg glass transition temperature to be a positive temperature at which the extrapolation reaches a vanishing width, that is, $T_{BG_1} = \beta - \overline{\Gamma}/\alpha$. We find positive T_{BG_1} defining the Bragg glass phase in all the intercalated samples, except that at the highest concentration ($x = 2.9\%$; Fig. 3f). The $x = 2.9\%$ sample appears to be fluctuating towards Bragg glass without actually reaching the Bragg glass phase. Combining the CDW-1 transition temperature T_{c1} of the pristine sample (Fig. 2d) and the newly extracted Bragg glass transition temperature, T_{BG_1}, of the intercalated samples (Fig. 3d–f shows data for 2.0%, 2.6% and 2.9%, respectively, and Supplementary Fig. 9a shows data for 0.5%), we obtain a comprehensive phase diagram (Fig. 3g). Remarkably, the temperatures identified from the onset of transport anisotropy[25] closely align with T_{BG_1}, implying that the phase space exhibiting in-plane resistance anisotropy is predominantly covered by the Bragg glass.

The impact of disorder in the intercalated samples is evidenced by CDW peak asymmetry[9,10,31,41] (Supplementary Section D). Due to the sharpness of the CDW peaks with their vanishing widths, comparing the peak height between two peaks is prone to pixelation error (Supplementary Section J). Hence, we focus on the asymmetry between the distribution of satellite scattering intensities across a Bragg peak. As shown in Fig. 4a,b, the contrast between the raw X-ray data from the pristine sample and the intercalated sample is stark. Specifically, although the pristine sample's intensity distribution shows minimal asymmetry of the satellite diffuse scattering across the Bragg peaks, the intercalated sample clearly shows enhanced asymmetry in the form of half-diamonds. The asymmetry is apparent as the congruent satellite points to these half-diamonds show no scattering. The raw intensity cuts (Fig. 4c,d) clearly show that the distribution of satellite intensities across a Bragg peak is uniquely asymmetric but only for the intercalated sample shown in Fig. 4d. We quantify the diffuse scattering asymmetry by the ratio α defined as $(I_1 - I_2)/(I_1 + I_2)$, where I_1 and I_2 are the corresponding intensities of the two congruent satellite diamond regions (Fig. 4e). The ratio α (Fig. 4e) quantifies the enhanced asymmetry in the intercalated samples and its absence in the pristine sample. The presence of asymmetry specific to the intercalated sample distinguishes it from the pristine sample and indicates the pinning of modulations in and around the CDW by the intercalant-induced disorder. A comprehensive picture of the prevalent asymmetry in the Bragg glass and short-range-ordered phase emerges on X-TEC clustering (Fig. 4f–h and Supplementary Fig. 9d). When the entire dataset of the intercalated sample is split into two clusters (after removing the Bragg peaks and CDW peaks), the clustering results reveal that the diffuse region around the satellite CDW-1 peaks is systematically asymmetric.

In summary, we report the first X-ray scattering evidence suggesting the existence of a Bragg glass phase in a family of disordered CDW systems, namely, Pd-intercalated $ErTe_3$. To disentangle the intrinsic phase fluctuation effects of CDW from crystalline imperfections despite finite experimental resolution, we obtained comprehensive XRD data spanning ~20,000 BZs over the 30–300 K temperature range. We then analysed the entire ~150 GB of XRD data using X-TEC, an unsupervised machine learning tool for revealing collective phenomena from voluminous temperature-dependent XRD data[24]. We employed a multifaceted approach of tracking three features, namely, peak height, peak width and asymmetry in satellite diffuse scattering, in the entire dataset. Consolidating the results of this analysis, we were able to disentangle the effects of lattice imperfections and finite momentum resolution from the intrinsic tendency for topological quasi-long-range order into a Bragg glass phase. We also observe that except for the pristine sample, there is an asymmetry in satellite diffuse scattering at all the intercalation levels, which indicates that all the intercalated samples have disorder pinning. We, thus, claim that even an infinitesimal intercalation introduces disorder and destroys the long-range order to a Bragg glass order. Thus, we discovered that for $x > 0$, the temperature and momentum dependence of the diffraction signal is consistent with the Bragg glass phase spanning most of the phase space that exhibits transport anisotropy, extending up to remarkably high temperatures. Future diffraction experiments at higher resolution and brightness can further confirm the Bragg glass nature of the anisotropic phase by detecting the power-law tails.

The impact of our findings is twofold. First, we made advances in understanding the elusive Bragg glass phase in a disordered CDW system from bulk diffraction data, by mapping the Bragg glass transition temperature estimates T_{BG} in the phase diagram. It is remarkable that the Bragg glass phase suggested from the absence of phase dislocations observed in the STM measurements[22] at temperatures below 1.7 K extends all the way up to 100.0 K and beyond until the Bragg glass phase collapses at around 2.9% intercalation. Moreover, the evidence for the Bragg glass we established leaves only a very narrow range of phase space that can possibly support the competing short-range-ordered phase. Second, the new discovery enabled by the use of X-TEC and the new high-throughput measure of peak width demonstrates the potential of the new machine-learning-enabled data analysis in addressing fundamental issues when intrinsic fluctuations and the effect of disorder lead to a complex and rich plethora of phenomena. Higher-intensity X-rays that can access many BZs often lead to worse signal-to-noise ratios. The high-throughput measure of peak width enabled us to disentangle the effects of crystalline defects from the effects of intrinsic CDW phase fluctuations by giving us access to zone-to-zone correlation in fluctuations over 20,000 BZs. This separation, in turn, allowed us to connect the voluminous XRD data with the STM observations and the theory of Bragg glasses. The modality of the comprehensive high-throughput extraction of theoretically inspired features promises to enable new discoveries in the era of big data, rich with information, and connect varied facets of complex systems accessible to different probes.

Online content

Any methods, additional references, Nature Portfolio reporting summaries, source data, extended data, supplementary information, acknowledgements, peer review information; details of author contributions and competing interests; and statements of data and code availability are available at https://doi.org/10.1038/s41567-023-02380-1.

References

1. Parisi, G. *Nobel Prize Lecture* (Nobel Prize Outreach AB, 2024); https://www.nobelprize.org/prizes/physics/2021/parisi/lecture/
2. Giamarchi, T. & Le Doussal, P. Elastic theory of pinned flux lattices. *Phys. Rev. Lett.* **72**, 1530–1533 (1994).
3. Giamarchi, T. & Le Doussal, P. Elastic theory of flux lattices in the presence of weak disorder. *Phys. Rev. B* **52**, 1242–1270 (1995).
4. Nattermann, T. Scaling approach to pinning: charge density waves and giant flux creep in superconductors. *Phys. Rev. Lett.* **64**, 2454–2457 (1990).
5. Gingras, M. J. P. & Huse, D. A. Topological defects in the random-field XY model and the pinned vortex lattice to vortex glass transition in type-II superconductors. *Phys. Rev. B* **53**, 15193–15200 (1996).
6. Kierfeld, J., Nattermann, T. & Hwa, T. Topological order in the vortex-glass phase of high-temperature superconductors. *Phys. Rev. B* **55**, 626–629 (1997).
7. Fisher, D. S. Stability of elastic glass phases in random field XY magnets and vortex lattices in type-II superconductors. *Phys. Rev. Lett.* **78**, 1964–1967 (1997).
8. Giamarchi, T. & Le Doussal, P. Phase diagrams of flux lattices with disorder. *Phys. Rev. B* **55**, 6577–6583 (1997).
9. Rosso, A. & Giamarchi, T. X-ray diffraction of a disordered charge density wave. *Phys. Rev. B* **68**, 140201 (2003).
10. Rosso, A. & Giamarchi, T. X-ray spectrum of a pinned charge density wave. *Phys. Rev. B* **70**, 224204 (2004).
11. Brazovskii, S. & Nattermann, T. Pinning and sliding of driven elastic systems: from domain walls to charge density waves. *Adv. Phys.* **53**, 177–252 (2004).
12. Doussal, P. L. in *BCS: 50 Years* (eds Cooper, L. N. & Feldman, D.) 277–336 (World Scientific, 2011).
13. Mross, D. F. & Senthil, T. Spin- and pair-density-wave glasses. *Phys. Rev. X* **5**, 031008 (2015).
14. Bogner, S., Emig, T. & Nattermann, T. Nonuniversal correlations and crossover effects in the Bragg-glass phase of impure superconductors. *Phys. Rev. B* **63**, 174501 (2001).
15. Klein, T. et al. A Bragg glass phase in the vortex lattice of a type II superconductor. *Nature* **413**, 404–406 (2001).
16. Bogner, S., Emig, T., Nattermann, T. & Scheidl, S. Comment on 'a Bragg glass phase in the vortex lattice of a type II superconductor'. Preprint at https://arxiv.org/abs/cond-mat/0110592 (2001).
17. Park, S. R., Choi, S. M., Dender, D. C., Lynn, J. W. & Ling, X. S. Fate of the peak effect in a type-II superconductor: multicriticality in the Bragg-glass transition. *Phys. Rev. Lett.* **91**, 167003 (2003).
18. Daniilidis, N. D., Park, S. R., Dimitrov, I. K., Lynn, J. W. & Ling, X. S. Emergence of quasi-long-range order below the Bragg glass transition. *Phys. Rev. Lett.* **99**, 147007 (2007).
19. Toft-Petersen, R., Abrahamsen, A. B., Balog, S., Porcar, L. & Laver, M. Decomposing the Bragg glass and the peak effect in a type-II superconductor. *Nat. Commun.* **9**, 901 (2018).
20. Altvater, M. A. et al. Observation of a topological defect lattice in the charge density wave of 1T-TaS_2. *Appl. Phys. Lett.* **119**, 121601 (2021).
21. Okamoto, J.-i., Arguello, C. J., Rosenthal, E. P., Pasupathy, A. N. & Millis, A. Experimental evidence for a Bragg glass density wave phase in a transition-metal dichalcogenide. *Phys. Rev. Lett.* **114**, 026802 (2015).
22. Fang, A., Straquadine, J. A. W., Fisher, I. R., Kivelson, S. A. & Kapitulnik, A. Disorder-induced suppression of charge density wave order: STM study of Pd-intercalated $ErTe_3$. *Phys. Rev. B* **100**, 235446 (2019).
23. Nie, L., Tarjus, G. & Kivelson, S. A. Quenched disorder and vestigial nematicity in the pseudogap regime of the cuprates. *Proc. Natl Acad. Sci. USA* **111**, 7980–7985 (2014).
24. Venderley, J. et al. Harnessing interpretable and unsupervised machine learning to address big data from modern X-ray diffraction. *Proc. Natl Acad. Sci. USA* **119**, e2109665119 (2022).
25. Straquadine, J. A. W., Weber, F., Rosenkranz, S., Said, A. H. & Fisher, I. R. Suppression of charge density wave order by disorder in Pd-intercalated $ErTe_3$. *Phys. Rev. B* **99**, 235138 (2019).
26. Imry, Y. & Ma, S.-k Random-field instability of the ordered state of continuous symmetry. *Phys. Rev. Lett.* **35**, 1399–1401 (1975).
27. Fang, A. et al. Robust superconductivity intertwined with charge density wave and disorder in Pd-intercalated $ErTe_3$. *Phys. Rev. Res.* **2**, 043221 (2020).
28. Ru, N. et al. Effect of chemical pressure on the charge density wave transition in rare-earth tritellurides RTe_3. *Phys. Rev. B* **77**, 035114 (2008).
29. Sinchenko, A. A., Grigoriev, P. D., Lejay, P. & Monceau, P. Spontaneous breaking of isotropy observed in the electronic transport of rare-earth tritellurides. *Phys. Rev. Lett.* **112**, 036601 (2014).
30. Krogstad, M. J. et al. Reciprocal space imaging of ionic correlations in intercalation compounds. *Nat. Mater.* **19**, 63–68 (2020).
31. Ravy, S. & Pouget, J. P. Structural studies of the CDW interaction with defects. *J. Phys. IV* **03**, C2-109–C2-114 (1993).
32. Zeng, C., Leath, P. L. & Fisher, D. S. Absence of two-dimensional Bragg glasses. *Phys. Rev. Lett.* **82**, 1935–1938 (1999).
33. Le Doussal, P. & Giamarchi, T. Dislocations and Bragg glasses in two dimensions. *Physica C* **331**, 233–240 (2000).
34. Rouzière, S., Ravy, S., Pouget, J.-P. & Brazovskii, S. Friedel oscillations and charge-density wave pinning in quasi-one-dimensional conductors: an X-ray diffraction study. *Phys. Rev. B* **62**, R16231–R16234 (2000).
35. Guinier, A. *X-Ray Diffraction: In Crystals, Imperfect Crystals, and Amorphous Bodies* (Dover Publications, 1994).
36. Emery, V. J. & Axe, J. D. One-dimensional fluctuations and the chain-ordering transformation in $Hg_{3-\delta}AsF_6$. *Phys. Rev. Lett.* **40**, 1507–1511 (1978).
37. Heilmann, I. U. et al. Neutron investigation of the dynamical properties of the mercury-chain compound $Hg_{3-\delta}AsF_6$. *Phys. Rev. B* **20**, 751–762 (1979).
38. Spal, R., Chen, C.-E., Egami, T., Nigrey, P. J. & Heeger, A. J. X-ray scattering study of one-dimensional lattice dynamics in $Hg_{3-\delta}AsF_6$. *Phys. Rev. B* **21**, 3110–3118 (1980).
39. Endres, H., Pouget, J. & Comes, R. Diffuse X-ray scattering and order-disorder effects in the iodide chain compounds *N*,*N*′-diethyl-*N*,*N*′-dihydrophenazinium iodide, $E_2PI_{1.6}$, and *N*,*N*′-diebenzyl-*N*,*N*′-dihydrophenazinium iodide, $B_2PI_{1.6}$. *J. Phys. Chem. Solids* **43**, 739–748 (1982).
40. Maki, K. Thermal fluctuations of the order parameter in charge-density waves. *Phys. Rev. B* **33**, 2852–2854 (1986).
41. Ravy, S. et al. Disorder effects on the charge-density waves structure in V- and W-doped blue bronzes: Friedel oscillations and charge-density wave pinning. *Phys. Rev. B* **74**, 174102 (2006).

Publisher's note Springer Nature remains neutral with regard to jurisdictional claims in published maps and institutional affiliations.

Open Access This article is licensed under a Creative Commons Attribution 4.0 International License, which permits use, sharing, adaptation, distribution and reproduction in any medium or format, as long as you give appropriate credit to the original author(s) and the source, provide a link to the Creative Commons license, and indicate if changes were made. The images or other third party material in this article are included in the article's Creative Commons license, unless indicated otherwise in a credit line to the material. If material is not included in the article's Creative Commons license and your intended use is not permitted by statutory regulation or exceeds the permitted use, you will need to obtain permission directly from the copyright holder. To view a copy of this license, visit http://creativecommons.org/licenses/by/4.0/.

© The Author(s) 2024

Methods

Synthesis

Samples were grown using a Te self-flux method[42]. Small amounts of Pd were included in the melt to produce the palladium-intercalated crystals. The produced crystals had an area of 1–2 mm^2 across and varied in thickness with the intercalation level. Since the CDW transition temperature is well characterized for different intercalation levels, resistivity measurements of the sample batches used were taken to determine the intercalation levels of the samples studied[25].

X-ray scattering

Samples were shipped to the Argonne National Laboratory in sealed vials filled with inert gas and removed and mounted on the tips of polyimide capillaries just before measurement to avoid degradation from water and oxygen exposure. During measurements, the samples were cooled using an Oxford N-Helix Cryostream, which surrounded the samples with either N_2 or He gas. The measurements were taken with incident X-ray energy of 87 keV in the transmission geometry, with samples continuously rotated at 1° s^{-1} and a PILATUS 2M CdTe detector taking images at 10 Hz. For each sample at each temperature, three such 365°-rotation scans were collected, with the detector slightly offset and the rotation angle slightly changed to fill in detector gaps and allow for the removal of detector artifacts[30].

Data analysis

The X-TEC package used for the analysis can be installed through the PyPI distribution, or from the source (https://github.com/KimGroup/XTEC). Supplementary Information provides further details regarding the data analysis.

Data availability

A dataset containing ~2,000 CDW peak features extracted by X-TEC for each intercalated sample and scripts to analyse them are available via Figshare at https://figshare.com/s/3058d505bfffed3a7436. All other data are available from the corresponding author upon request.

Code availability

All the codes used for the analysis are available at https://github.com/KimGroup/PdxErTe3_XTEC_analysis.

References

42. Ru, N. & Fisher, I. R. Thermodynamic and transport properties of YTe_3, $LaTe_3$, and $CeTe_3$. *Phys. Rev. B* **73**, 033101 (2006).

Acknowledgements

This work was supported by the US Department of Energy, Office of Basic Energy Sciences, Division of Materials Sciences and Engineering, and used resources of the Advanced Photon Source, a US Department of Energy, Office of Science User Facility, at Argonne National Laboratory. The initial X-TEC analysis on the pristine sample was carried out on the Red Cloud at the Cornell University Center for Advanced Computing, with support from the Department of Energy under award DE-SC0018946. The X-TEC analysis on the intercalated samples was carried out on the high-powered computing cluster funded in part by the Gordon and Betty Moore Foundation's EPiQS Initiative, grant GBMF10436 (to E.-A.K.), and by the New Frontier Grant from the College of Arts and Sciences at Cornell (to E.-A.K.). K.M. was supported by Eric and Wendy Schmidt AI in Science Postdoctoral Fellowship, a Schmidt Futures programme. Work at Stanford University (crystal growth and characterization, and contributions to the diffraction experiments) was supported by the Department of Energy, Office of Basic Energy Sciences, under contract DE-AC02-76SF00515.

Author contributions

J.S., M.D.B. and A.G.S., supervised by I.R.F., prepared the samples. X-ray experiments and data processing were performed by M.J.K., J.S., R.O. and S.R. K.M. and E.-A.K. developed and implemented the machine learning analysis and interpreted the results with guidance and feedback from I.R.F., M.J.K., S.R. and R.O. K.M. and E.-A.K. wrote the manuscript with critical inputs from M.J.K., R.O., I.R.F. and all other authors.

Competing interests

The authors declare no competing interests.

Additional information

Supplementary information The online version contains supplementary material available at https://doi.org/10.1038/s41567-023-02380-1.

Correspondence and requests for materials should be addressed to Eun-Ah Kim.

Peer review information *Nature Physics* thanks Pratap Raychaudhuri, Rasmus Toft-Petersen and the other, anonymous, reviewer(s) for their contribution to the peer review of this work.

Reprints and permissions information is available at www.nature.com/reprints.